Stacking Fault Induced Symmetry Breaking in van der Waals Nanowires

Eli Sutter,[1,2] Hannu-Pekka Komsa,[3] Alexander A. Puretzky,[4] Raymond R. Unocic,[4] and Peter Sutter[5,*]

[1]Department of Mechanical and Materials Engineering, University of Nebraska-Lincoln, Lincoln, NE 68588, United States

[2]Nebraska Center for Materials and Nanoscience, University of Nebraska-Lincoln, Lincoln, NE 68588, United States

[3]Faculty of Information Technology and Electrical Engineering, University of Oulu, FI-90014, Oulu, Finland

[4]Center for Nanophase Materials Sciences, Oak Ridge National Laboratory, Oak Ridge, TN 37830, United States

[5]Department of Electrical and Computer Engineering, University of Nebraska-Lincoln, Lincoln, NE 68588, United States

[*]Corresponding author, e-mail: psutter@unl.edu

Abstract

While traditional ferroelectrics are based on polar crystals in bulk or thin film form, two-dimensional and layered materials can support mechanisms for symmetry breaking between centrosymmetric building blocks, *e.g.*, by creating low-symmetry interfaces in van der Waals stacks. Here, we introduce an approach toward symmetry breaking in van der Waals crystals that relies on the spontaneous incorporation of stacking faults in a non-polar bulk layer sequence. The concept is realized in nanowires consisting of Se-rich group IV monochalcogenide ($GeSe_{1-x}S_x$) alloys, obtained by vapor-liquid-solid growth. The single crystalline wires adopt a layered structure in which the non-polar A-B bulk stacking along the nanowire axis is interrupted by single-layer stacking faults with local A-A' stacking. Density functional theory explains this behavior by a reduced stacking fault formation energy in GeSe (or Se-rich $GeSe_{1-x}S_x$ alloys). Computations demonstrate that, similar to monochalcogenide monolayers, the inserted A-layers should show a spontaneous electric polarization with a switching barrier consistent with a Curie temperature above room temperature. Second-harmonic generation signals are consistent with a variable density of stacking faults along the wires. Our results point to possible routes for designing ferroelectrics *via* the layer stacking in van der Waals crystals.

Keywords: Layered crystals, germanium selenide, germanium sulfide, alloy, planar defects, electron microscopy, van der Waals stacking

Ferroelectrics, *i.e.*, materials with a spontaneous electric polarization that can be reversed by the application of an external electric field, typically adopt a polar space group in the bulk. Prototypical ferroelectrics are 3D perovskite oxides such as barium titanate in which asymmetric shifts in the equilibrium ion positions give rise to a non-centrosymmetric crystal structure with a permanent, electrically switchable dipole moment. 2D and layered van der Waals crystals are attractive materials for the search for unconventional ferroelectrics, combining attributes such as tunable thickness down to a single layer and chemically inert surface termination. In the monolayer limit, a number of 2D materials crystallize in reduced symmetry structures that support in some cases out-of-plane ($MoTe_2$)[1] but mostly in-plane polarization (In_2Se_3,[2] SnS,[3-4] SnSe).[5] In the few-layer to bulk regime, van der Waals crystals that comprise centrosymmetric layers but whose stacking sequence breaks inversion symmetry, such as WTe_2[6] have so far remained the exception. For most layered crystals including transition metal dichalcogenides (TMDs), hexagonal boron nitride and others, the equilibrium stacking sequence has inversion symmetry so that these layered materials are not ferroelectric in the bulk. In TMDs, replacing the most common 2H polymorph by a rhombohedral 3R stacking sequence provides a pathway to non-centrosymmetric layered crystals.[7-8] Another possible approach to overcome this issue involves interfacial symmetry breaking *via* stacking of non-isotypic or isostructural 2D crystals, which has been shown to produce a bulk photovoltaic response in WSe_2 and black phosphorus heterostacks[9] as well as out-of-plane ferroelectricity in MoS_2/WS_2 heterobilayers.[10] Another way of breaking inversion symmetry, recently demonstrated for bilayer hBN,[11-12] entails stacking layers in a non-equilibrium registry. However, these types of interfacial engineering are generally limited to mechanically stacked 2D layers; bottom-up synthesis of non-isotypic stacks faces compatibility issues, while growth of non-equilibrium shifted or twisted stacks is challenging due to the tendency of the layers to realign or shift back toward their (centrosymmetric) equilibrium stacking registry.

Here, we introduce a different approach to symmetry breaking in van der Waals materials: the introduction of stacking faults with reduced symmetry in a centrosymmetric stacked host crystal. We demonstrate this concept for the example of nanowires of group IV monochalcogenides (MX, where M = Sn, Ge; X = S, Se), anisotropic van der Waals crystals that are binary analogues of black phosphorus.[13] MX monochalcogenides have been pursued as ferroelectrics following the theoretical prediction of multiferroic order with coupled in-plane ferroelectricity and ferroelasticity above room temperature.[14-19] However, group IV monochalcogenides present significant challenges for realizing ferroelectricity. Individual 2D

layers crystallize in an anisotropic non-centrosymmetric structure and have for SnS and SnSe demonstrated ferroelectric polarization.[3-5] However, monolayers of these materials have remained difficult to obtain both by exfoliation and growth. In the few-layer regime, symmetry breaking is also challenging to obtain experimentally. The crystal structure of the entire MX family is orthorhombic (space group *Pnma*) with puckered layers arranged in A-B equilibrium stacking sequence (Figure S1).[5,14,17,20-22] Ferroelectricity is thickness dependent since in the centrosymmetric A-B stacking only an odd layer number breaks the compensation between A and B layers to give rise to a net electric polarization. Such precise control over the number of layers is evidently hard to achieve.

While the pure group IV monochalcogenides have been experimentally prepared as flakes,[4,23-27] ribbons,[28] and nanowires,[29-30] alloys with mixed cations (Ge, Sn), anions (S, Se), or both, have been far less reported. Ge-based monochalcogenide alloys have been limited to nanoparticles.[31] It is expected that both the structure and properties of alloys will bridge between the pure endpoint materials, *e.g.*, GeS and GeSe for $GeSe_{1-x}S_x$ alloys. GeS nanowires synthesized by a vapor-liquid-solid (VLS) process have gained prominence for optoelectronics,[30] nanophotonics,[32] and 3D twistronics.[33] GeSe, of interest for photovoltaics and optoelectronic applications due to its 1.3 eV direct band gap,[34] high carrier mobility,[35] and excellent environmental stability, also lends itself to VLS growth, albeit in the form of large ribbons.[36] Our present results show that VLS growth of Se-rich $GeSe_{1-x}S_x$ alloys produces nanowires in which the centrosymmetric equilibrium A-B stacking sequence is interrupted by incorporation of monolayer stacking faults with metastable A-A' stacking, *i.e.*, the insertion of an additional A-layer with a ½ unit cell shift along the ***b***-direction (Figure S1). Density functional theory (DFT) confirms lower formation energies for such metastable A-A' stacking in GeSe compared to GeS, and it shows that the observed A-A' stacking faults have lower energy than an A-A stacking sequence with laterally aligned A-layers. *Ab-initio* calculations demonstrate that the symmetry breaking due to this local A-A' stacking gives rise to ferroelectricity analogous to a single MX monolayer.[3-4] The reduced symmetry in areas with high densities of stacking faults is observable experimentally *via* second harmonic generation. Our results identify symmetry breaking due to stacking faults in otherwise centrosymmetrically stacked MX nanowires as a possible avenue toward van der Waals ferroelectrics.

Results and Discussion

Ge-Se-S nanostructures were grown in a quartz tube reactor with two independently controlled temperature zones by simultaneous evaporation of GeS and GeSe powders using Ar as a carrier gas (see Methods for details). Au-catalyzed VLS growth from a pure GeSe precursor yields macroscopically large, single-crystalline GeSe ribbons that crystallize in a layered structure, with *c*-axis (*i.e.*, the van der Waals stacking direction) perpendicular to the ribbon axis (Figure S2),[36] similar to GaS and GaSe nanoribbons reported earlier.[37-38] Adding GeS vapor *via* simultaneous evaporation of GeSe and GeS precursors leads to the formation of nanowires that are stacked with the *c*-axis parallel to the wire axis. TEM images of the nanowires formed at the lowest GeS vapor pressure used in our experiments are shown in **Figure 1**. The nanowires grow up to several tens of micrometers long and appear tapered with diameters decreasing toward their tips. Hemispherical caps at their tips show characteristic darker TEM (see also Figure S3) and brighter HAADF-STEM (Figure S4) contrast, consistent with a Au-rich VLS catalyst particle. High-resolution TEM (Figure 1 (d)) and nanobeam electron diffraction (Figure 1 (e)-(f)) show that the nanowires are single crystals with the same orthorhombic layered structure (space group *Pnma*) found for GeSe[39-40] and GeS.[40] The TEM images and electron diffraction patterns confirm that the nanowire axis lies along the [001] direction, *i.e.*, the *c*-axis is aligned with the nanowire axis. Lattice fringes in high-resolution TEM (Figure 1 (d)) are separated by ~0.545 nm perpendicular to the nanowire axis,

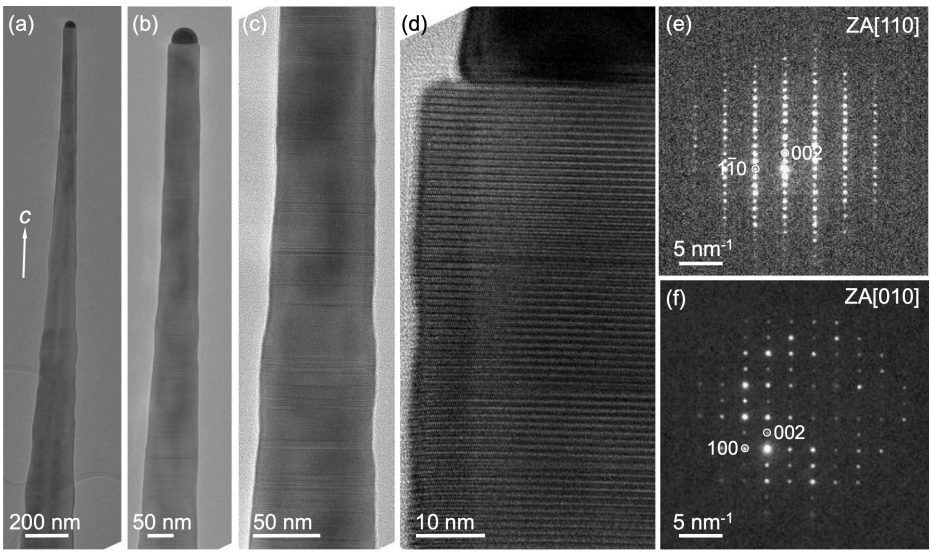

Figure 1. Morphology of Au-catalyzed nanowires from GeSe and GeS vapors at P_{GeSe} = 5.6 ×10^{-3} Torr and P_{GeS} = 5.6 ×10^{-2} Torr. **(a)** TEM image of a characteristic nanowire grown over Au catalyst at a substrate temperature of 300°C (dispersed on lacey carbon support). **(b)** TEM image close to the nanowire tip**. (c)** Higher magnification TEM image of a section of the nanowire. **(d)** High-resolution TEM image of a nanowire near the tip. **(e) – (f)** Nanobeam electron diffraction patterns of the wire along the [110] and [010] zone axes (ZA), respectively.

consistent with the spacing of (002) planes in bulk GeSe and GeS.[40] The lattice constants of the nanowires determined from the electron diffraction (a = 3.857 Å, b = 4.399Å, c = 10.898 Å) are smaller than for pure GeSe (a = 3.878 Å, b = 4.550 Å, c = 11.142 Å), as expected due to alloying by incorporation of GeS.

Chemical analysis by energy-dispersive X-ray spectroscopy (EDS) in scanning electron microscopy (SEM) detects Ge, Se, and S, *i.e.*, demonstrates incorporation of S in the $GeSe_{1-x}S_x$ alloy nanowires (**Figure 2**). Quantitative EDS analysis of several nanowires yields an average S content of 5-7 at. %, confirming Se-rich $GeSe_{0.9}S_{0.1}$ nanowires. Elemental maps show a uniform distribution of Ge, Se, and S. The intensity of the S signal is relatively low (Figure 2 (d)), but EDS spectra (Figure 2 (e)) consistently show a pronounced S peak. Au is limited to the catalyst particle at the nanowire tip (see Figure S3). A detailed TEM characterization (Figure S4) confirms that the catalyst tips consist of single-crystalline Au.

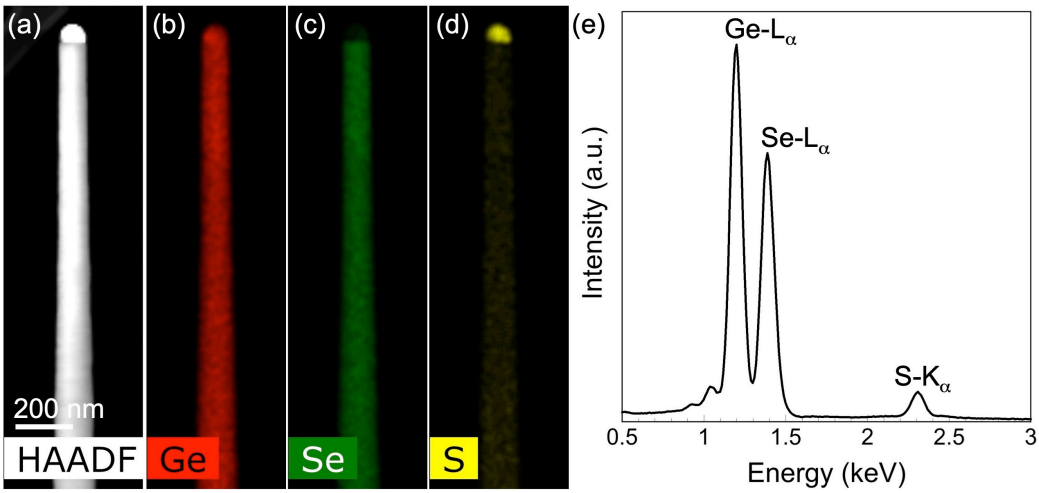

Figure 2. Chemical analysis of nanowires grown from GeSe and GeS vapor at vapor pressures P_{GeSe} = 5.6 ×10^{-3} Torr and P_{GeS} = 5.6 ×10^{-2} Torr. (a) HAADF-STEM image of a segment of a representative nanowire. **(b) – (d)** EDS maps of the nanowire showing the distribution of Ge ((b), red), Se ((c), green), and S ((d), yellow). **(e)** EDS spectrum from the nanowire.

Importantly, both TEM (Figure 1, **Figure 3**) and HAADF-STEM (Figure S5) show a non-uniform, striped contrast in the nanowires. Similar stripes have been observed in III-V semiconductor nanowires, where they are associated with changes between zincblende and wurtzite polymorphs.[41] High-resolution (HR) TEM imaging of the morphology of a characteristic $GeSe_{1-x}S_x$ nanowire (Figure 3 (a) – (b)) shows segments with uniform contrast interrupted by inclusion of a single layer with different contrast. HRTEM of the uniform segments (Figure 3 (c), zone axis, ZA: [110]) shows the characteristic atomic structure of layered $GeSe_{0.9}S_{0.1}$ with equilibrium A-B stacking, confirmed by an excellent match between the experimental image and a multislice image simulation (Figure 3 (c), right) for the A-B

stacked layer structure. Nanobeam electron diffraction (Figure 3 (c')) also confirms the A-B stacking in this segment (see also Figure S6). Occasionally the periodic layered structure is disrupted, *i.e.*, one layer spacing appears larger (Figure 3 (d)). At this position a single stacking fault is inserted into the A-B stacked nanowire. Prior work has identified an alternative A-A stacking sequence in the group IV monochalcogenide SnS,[3] where the sequence of alternating A- and B-layers is replaced by repeated A-layers that align across the van der Waals gap (Figure S1). We considered the insertion of an A-A layer pair as a possible structure of the stacking faults in our nanowires (Figure 3 (e)). However, several characteristics do not match those expected for an A-A stacking fault: (i) Although the contrast in HRTEM is consistent with the insertion of an additional A-layer, [110] ZA images do not show the expected registry (*i.e.*, lateral alignment of the A-layers, Figure 3 (d)); (ii) similarly, atomically resolved HAADF-STEM along [110] ZA shows two consecutive A-

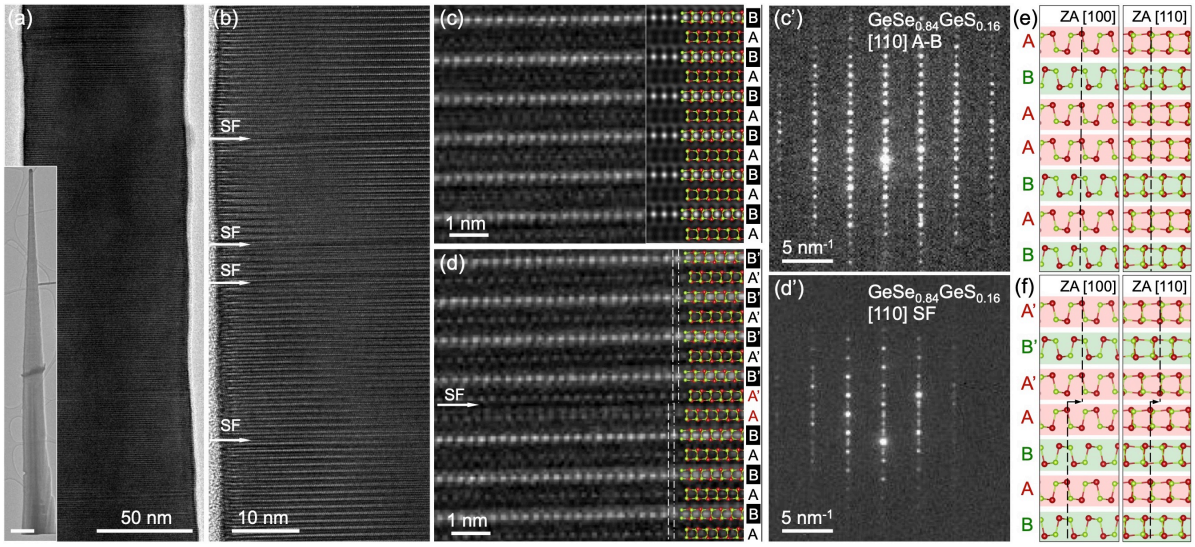

Figure 3. Stacking faults in $GeSe_{1-x}S_x$ nanowires with S content below 15 at.%. (a) TEM image of a section of a characteristic $GeSe_{0.9}S_{0.1}$ nanowire. Inset: TEM image of the entire nanowire; scale bar: 500 nm. **(b)** High-resolution TEM image showing the stacking of the van der Waals layers. SF: Single stacking faults inserted in the A-B stacked nanowire. **(c)** Higher magnification view of the lattice fringes in one of the extended segments with equilibrium A-B stacking. Right: Multislice image simulation with overlaid atomic positions. **(d)** Higher magnification view of the lattice fringes around a stacking fault in (b), with atomic positions indicated based on the multislice simulation in (c). Vertical dashed and dash-dotted lines indicate a shift of the A- and B-layer lattices to the right across the stacking fault, a telltale signature of a A-A' stacking fault seen along the [110] zone axis (see panel (f)). **(c') – (d')** Nanobeam electron diffraction patterns along the [110] ZA, obtained in an A-B stacked segment (c) and at the stacking fault in (d). See Figure S5 for a comparison with diffraction simulations. **(e)** Model of the A-B stacked structure hosting an A-A stacking fault. **(f)** Model of the A-B stacked structure hosting an A-A' stacking fault, where the layers after the stacking defect are shifted by ***b***/2. This shift along the ***b***-axis results in a smaller displacement in [110] zone axis view.

layers at the stacking fault shifted laterally by ~¼ unit cell (Figure S7); and (iii) [110] ZA nanobeam electron diffraction shows the suppression of $[1\bar{1}0]$ and $[\bar{1}10]$ reflections that should be present in A-A stacking (Figure 3 (d'), Figure S6). These signatures are consistent with a different, not previously identified layer sequence at the stacking fault, which we call A-A' stacking (Figure 3 (f)). In the A-A' stacking, consecutive A-layers are shifted by ½ unit cell in the ***b***-direction (Figure S1). In a [110] view, this translates into a lateral shift by ~¼ $[\bar{1}10]$ unit cell, as observed in HRTEM and HAADF-STEM of individual stacking faults. This implies that the following A-B stacked layers inherit their registry from the A'-layer at the stacking fault, *i.e.*, are also laterally shifted relative to the A-B stack prior to the fault (Figure 3 (d), (f)). Furthermore, the simulated electron diffraction pattern for A-A' stacking coincides with the DPs observed at single stacking faults in our nanowires. As we will discuss below, DFT calculations show the A-A' stacking fault as energetically favorable compared to the A-A structure. We conclude that the observed stripe pattern in the $GeSe_{0.9}S_{0.1}$ nanowires stems from individual A-A' stacking faults incorporated in a host crystal with overall A-B stacking. Importantly, the local A-A' stacking (*i.e.*, insertion of an additional A'-layer) breaks the mirror symmetry of the equilibrium (A-B stacked) monochalcogenide structure.

We note that, apart from their inverted electric dipoles, there is no fundamental distinction between the A- and B-layers in A-B stacked monochalcogenides (Figure S1). Hence, there should be A-A' as well as B-B' stacking faults in our $GeSe_{1-x}S_x$ nanowires, and if adjacent stacking faults are non-interacting (*i.e.*, statistically independent), the probability of inserting either an extra A'- or B'-layer should be equal (50%). We used HRTEM images with consistent contrast over nearly 100 nm (~100 unit cells) to test this hypothesis (Figure 4). Along [100] ZA and with the chosen defocus, A- and B-layers appear with characteristic dark and bright contrast, respectively (Figure 4 (a), (b)), and are thus readily identified in intensity profiles across large distances. The profile shown in Figure 4 (c) contains seven stacking faults over ~80 nm, of which five are monolayer A-type, one is an A-type double-fault, and one is B-type. Importantly, we find five consecutive A-type stacking faults. For non-interacting defects, this sequence should be highly improbable (probability ~3.1 %). These findings suggest that the selection of the additionally inserted layer during growth is not random, but is biased toward forming consecutive stacking faults of the same type. Establishing the underlying mechanism will require additional work, but possible explanations include energy minimization *via* formation of a ferroelectric domain structure, elastic interaction, or another type of bias arising during the growth process.

Stacking faults persist in the layered alloy nanowires to sulfur concentrations up to 15 at.% (*i.e.*, $GeSe_{0.7}S_{0.3}$). Figure S8 shows a typical $GeSe_{0.72}S_{0.28}$ nanowire containing stacking faults within an A-B stacked host crystal. Upon further increase of the sulfur content, the stacking faults in the $GeSe_{1-x}S_x$ nanowires decrease, and wires with S concentration of ~30 at.% ($GeSe_{0.4}S_{0.6}$) and above no longer incorporate stacking faults (Figure S9). These wires

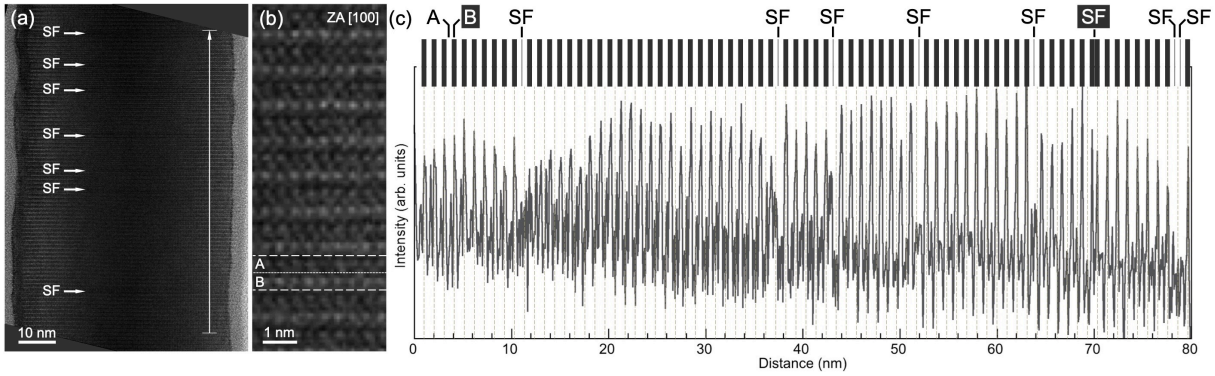

Figure 4. Analysis of a sequence of stacking faults (SF) from large-scale high-resolution TEM. (a) High-resolution TEM image of a $GeSe_{0.9}S_{0.1}$ nanowire with consistent contrast over nearly 100 nm. Zone axis (ZA): [100]. **(b)** Higher magnification of the observed lattice fringes in an A-B stacked part of the wire. Dashed horizontal lines (spaced ~1 nm) indicate a ***c***-axis unit cell. The thinner dotted line separates A- and B-layers. **(c)** Intensity profile along the line shown in (a), where the largest peaks coincide with the center of the B-layers while less intense maxima coincide with the A-layers. Dashed vertical lines indicate consecutive unit cells along the ***c***-axis (*i.e.*, van der Waals stacking direction). The seven stacking faults along this line comprise a sequence of five A-type faults, one B-type fault, and one A-type double fault. For uncorrelated (*i.e.*, non-interacting) stacking faults, the probability of obtaining five consecutive A-A' faults is $1/2^5 = 3.1$ %.

are longer, have uniform diameters, and they harbor axial screw dislocations, similar to pure GeS nanowires.[29,42] Similar to GeS wires, they can also transition from a major dislocated segment with diameter-dependent Eshelby twist to a layered (non-dislocated) section close to the tip (Figure S9(b)).[42]

Additional EDS experiments were performed to probe if stacking faults in $GeSe_{1-x}S_x$ nanowires are accompanied by differences in Se/S content (see Figure S10). EDS linescans across alternating regions with low and high stacking fault density show no detectable correlation between the ratio of Se to S concentrations and the local abundance of stacking faults (Figure S10 (a), (b)). Hence, aside from the effects of the overall S content in the alloy, discussed above, there is no apparent link between the chemical composition and the introduction of stacking faults.

In summary, growth by simultaneous exposure to GeSe and GeS vapors causes a switch in morphology from nanoribbons, obtained from a pure GeSe precursor, to tapered $GeSe_{1-x}S_x$ alloy nanowires with A-A' stacking faults, and ultimately (for S content above 30 at.%)

twisted $GeSe_{1-x}S_x$ nanowires. Additional electron microscopy suggests that stacking faults also exist in pure GeSe nanostructures, consistent with their low formation energy in Se-rich Ge monochalcogenides (Figure S10). Characteristic Au catalyst particles at the tips of the $GeSe_{1-x}S_x$ nanowires suggests that, similar to layered GeS nanowires,[30] their growth proceeds via a VLS process. Prior work has shown that vapor-phase additives can change the VLS catalyst drop and influence the morphology of a growing nanostructure without necessarily being incorporated. For instance, adding small amounts of SnS to the primary GeS precursor tunes the layer orientation in GeS nanowires without detectable Sn incorporation.[43] Similarly, adding small amounts of GeS to the GeSe vapor switches the morphology from nanoribbon to nanowire while also inducing chalcogen substitution. For GeS concentrations between ~5–50 at. %, the nanowire morphology is maintained while the wires become $GeSe_{1-x}S_x$ alloys whose composition is tunable *via* the ratio between GeS and GeSe precursor vapor pressures all the way to pure GeS (x = 1, Figure S12). DFT calculations support this observed isomorphous behavior, *i.e.*, complete miscibility over the entire range of compositions even at room temperature. Both theory (Figure S13, Figure S14) and electron diffraction measurements (Figure S12) confirm Vegard's law, *i.e.*, a linear change in the lattice constants of the $GeSe_{1-x}S_x$ alloys between GeSe and GeS.

The observed tendency toward incorporation of single A-A' stacking faults in the otherwise A-B stacked nanowires at high Se content implies a local lifting of the inversion symmetry of the A-B bilayer structure and thus warrants further consideration. To understand the origin of these spontaneous changes in the stacking order, we performed DFT calculations evaluating the formation energies for the equilibrium A-B and the metastable A-A and A-A' stacking in GeS and GeSe (Figure S15). The calculations (see Table S1) show that in GeSe, the energy differences between A-A and A-B stacking (0.023 eV per monolayer (ML) unit cell) and between A-A' and A-B stacking (0.048 eV per ML unit cell) are small, while they are significant in GeS (0.146 eV and 0.079 eV per ML unit cell, respectively). If the in-plane lattice constants are fixed to those of the A-B phase and the out-of-plane lattice constant is optimized, which should correspond more closely to the experimental situation, the energy differences increase to 0.115 eV per ML unit cell (GeSe, A-A), 0.070 eV per ML unit cell (GeSe, A-A'), 0.191 eV per ML unit cell (GeS, A-A), and 0.094 eV per ML unit cell (GeS, A-A'), respectively. We find that these values provide good approximations to the energy of a stacking fault from calculations with a single A-A' stacking fault introduced within a thick slab of A-B phase (0.069 eV and 0.102 eV for GeSe and GeS, respectively), and the A-A' stacking fault is in all cases lower in energy than the A-A type (Figure S16). Thus, we

conclude that the introduction of stacking faults is easier in GeSe and therefore favored at Se-rich alloy compositions, consistent with our experimental results. Additional calculations for varying number of A-B stacked cladding layers or number of A-A stacking faults (Figure S16) show that these conclusions are robust across a wide range of layer configurations. Considering the effects on the electronic structure, we find that both A-A' and A-A stacking faults are electronically benign without causing deep-level defect states in the gap (Figure S17).

To assess the possibility of a spontaneous ferroelectric polarization due to the symmetry breaking at stacking faults, we used DFT to compute the electronic contribution to the polarization by using the modern theory of polarization based on the Berry phase. The actual Se-rich $GeSe_{1-x}S_x$ alloys of our nanowires were approximated as pure GeSe. To validate the calculations, we computed the spontaneous polarization and transition state energy for a GeSe

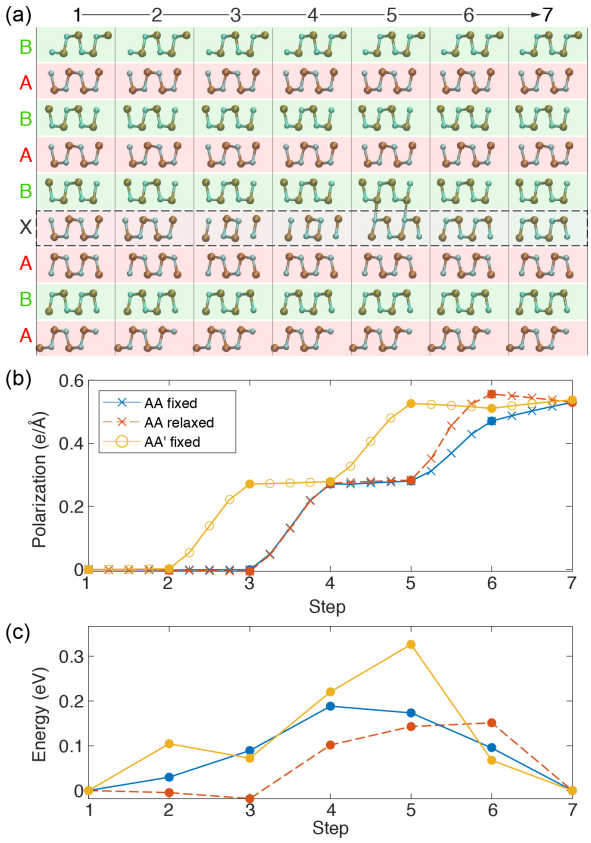

Figure 5. ***Ab-initio*** **calculation of ferroelectric polarization switching of A-A and A-A' stacking faults embedded in A-B stacked GeSe. (a)** Atomic structures along the transformation path of an A-A' stacking fault ('X') within an A-B stacked host crystal, as found experimentally. **(b)** Computed polarization along the transformation pathway (7 steps, see (a)). In the 'fixed' case, the positions of atoms in the neighboring layers are frozen, while in the 'relaxed' scenario all atoms are allowed to move. The final polarization (0.54 e/Å for an A-A' stacking fault) is consistent with but somewhat larger than the polarization for a MX monolayer (0.44 e/Å, see Figure S18). **(c)** Energy landscape along the transformation path for 'fixed' (A-A and A-A') and 'relaxed' (A-A) cases from nudged elastic band calculations.

monolayer (Figure S18), finding excellent agreement with published results.[17] **Figure 5** shows results of nudged elastic band calculations for the electric polarization and energy along the transformation path for switching of the embedded stacking fault from an initial A-A' to a final B-B' configuration (Figure 5 (a)). Calculations were performed for two scenarios: *(i)* In the 'fixed' case, the positions of all atoms in neighboring layers were frozen; *(ii)* in the 'relaxed' case, the positions of all atoms were optimized, which resulted in significantly slower convergence. The resulting polarization, ΔP, and energy profile along the transformation path are shown in Figure 5 (b) and Figure 5 (c), respectively. For the experimentally identified A-A' stacking fault, we find ΔP = 0.54 e/Å between states 1 and 7 in Figure 5 (a), which yields a spontaneous polarization P_S = ½ ΔP = 4.32×10^{-10} C/m, equal to that of a B-B' stacking fault and somewhat larger than P_S for a monolayer (3.53×10^{-10} C/m, Figure S18). Energy barriers for the transformation of 362 meV (A-A', fixed), 190 meV (A-A, 'fixed'), and 150 meV (A-A, 'relaxed') are also higher than for switching of a monolayer (103 meV, Figure S16), suggesting that the embedding in an A-B stacked host crystal tends to raise the Curie temperature beyond the value of the monolayer ferroelectric (estimated to lie well above room temperature).[17]

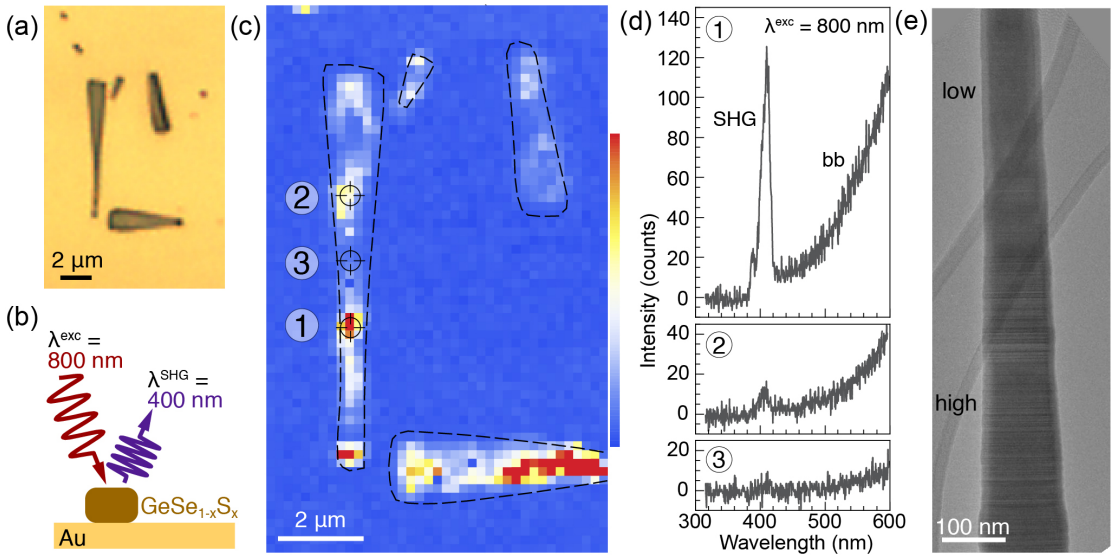

Figure 6. Second-harmonic generation (SHG) in Se-rich $GeSe_{1-x}S_x$ nanowires. (a) Optical microscopy image of a group of $GeSe_{1-x}S_x$ nanowires transferred to Au/Si support. **(b)** Schematic of the SHG experiment using exciting laser light with wavelength λ^{exc} = 800 nm converted to its second-harmonic (λ^{SHG} = 400 nm) by the non-centrosymmetric structure at stacking faults. **(c)** SHG intensity map displaying the intensity in the wavelength window between 390 – 410 nm. **(d)** Spectra obtained at points (1) – (3) marked in the map shown in (c). Note the coexistence of the SHG signal with a background signal due to blackbody (bb) radiation due to heating of the wires by the laser. **(e)** TEM image showing alternating areas with high and low density of stacking faults along the $GeSe_{1-x}S_x$ nanowires.

We used second harmonic generation (SHG) spectroscopy to assess if the local symmetry breaking near A-A' stacking faults can be detected experimentally. The experiments performed on dry-transferred wires on Au/Si supports (**Figure 6** (a)) used incident ultrafast laser pulses at 800 nm wavelength (Figure 6 (b); see Methods for details). SHG was performed on nanowires from the same samples as the wires imaged by electron microscopy, and the identical morphology and consistent presence of stacking faults (and absence of other defects, *e.g.*, dislocations) in all nanowires imaged by (S)TEM strongly suggests the non-centrosymmetric structure at the stacking faults as the origin of SHG signal.

A typical SHG map is shown in Figure 6 (c), where the integrated intensity in a narrow wavelength window (390 – 410 nm) centered at the second harmonic is plotted. The measurements show areas of high SHG intensity alternating with lower signals in each of the wires in a small group. The different signals can be seen in the example spectra obtained at different positions within one of the wires (Figure 6 (d)). Note that in addition to the SHG signal at 400 nm, there is a substantial intensity of emitted light across the visible spectrum. We ascribe this emission to blackbody radiation due to the heating of the nanowires by the exciting laser pulses, consistent with the absorption of the 800 nm light by the $GeSe_{1-x}S_x$ alloy nanowires (Figure S19). The existence of SHG intensity minima down to near zero intensity corroborates that second harmonic generation does not originate from nanowire geometry or surface effects, but indeed reflects the symmetry breaking by stacking faults along the wires. Since SHG signal is only expected for non-centrosymmetric stacking while it vanishes in A-B stacked parts of the sample, the strong variations in SHG intensity can be understood as resulting from different local densities of stacking faults along the nanowires, which are evident in our structural characterization (Figure 6 (e)).

Conclusions

Local symmetry breaking at stacking faults in otherwise centrosymmetrically stacked crystals represents a possible avenue toward inducing ferroelectricity in layered materials. Here, we demonstrated the realization of this concept for nanowires of Ge-based group IV monochalcogenides. While vapor-liquid-solid (VLS) growth from pure GeS yields nanowires with a chiral twisted structure around an axial screw dislocation and VLS growth from GeSe produces large nanoribbons, VLS growth of Se-rich $GeSe_{1-x}S_x$ alloys gives rise to semiconducting 1D nanostructures with mixed characteristics, adopting the morphology of layered nanowires found for GeS (albeit without a screw dislocation) while inheriting from GeSe the tendency to form stacking faults. This results in layered van der Waals nanowires

comprising single-layer A-A' stacking faults embedded in an A-B stacked host crystal. Similar to a single monolayer or few-layer crystals with odd layer number, the stacking fault layers break the inversion symmetry of the equilibrium A-B stacked bulk. Calculations suggest that this symmetry breaking results in robust ferroelectricity with spontaneous polarization at least on par with that of group IV monochalcogenide monolayers and switching barriers consistent with Curie temperatures well above room temperature. Second harmonic generation spectroscopy, which shows regions with different second harmonic intensity alternating along the wires, provides an experimental confirmation of the local symmetry breaking by A-A' stacking faults. The prospect of incorporating layers that carry a spontaneous electric polarization in anisotropic van der Waals nanowires promises flexibility in the choice of the polarization axis not found in planar thin film ferroelectrics. Specifically, in wires supported on a substrate, the electric dipole may be oriented continuously between in-plane and out-of-plane polarization by rotating the wire around its axis (Figure S20). If the elementary dipoles due to individual stacking faults are aligned parallel to one another (as they would be in our $GeSe_{1-x}S_x$ alloy nanowires), such a continuous reorientation might be effected by an applied electric field, providing opportunities for manipulating the electric polarization.

Methods

Experimental Methods: $GeSe_{1-x}S_x$ nanowires were synthesized using GeSe and GeS powders (99.99%; ALB Materials) in an experimental setup consisting of a pumped quartz tube reactor with two temperature zones. The GeSe and GeS precursors were placed in separate quartz boats in the evaporation zone and heated to temperatures between 400 – 450°C. Nanowires containing 5-6 at. % S were prepared under the following conditions: GeSe: 450°C, P_{GeSe} = 5.6×10^{-3} Torr; and GeS: 400°C, P_{GeS} = 0.0556 Torr. Alloy nanowires with higher sulfur content were prepared at higher GeS vapor pressures; here, the GeSe powder was heated to 400°C ($P_{GeSe} = 6.08 \times 10^{-4}$ Torr), while the GeS temperature was varied between 400 – 450°C (P_{GeS} between 0.0556 – 0.288 Torr). Si(100) covered with 2 nm thick Au films deposited by sputtering at room temperature was used as substrate. In all experiments the zone containing the substrate was heated to a growth temperature of 300°C. During growth, an Ar (99.9999%, Matheson) carrier gas flow was maintained at 60 standard cubic centimeters per minute (sccm) at a pressure of 20 mTorr. The growth was typically performed for 5 minutes, resulting in the formation of forests of nanowires with lengths of several tens of micrometers. Structure and morphology of the nanowires were investigated by transmission electron microscopy

(TEM) in an FEI Talos F200X microscope on nanowires spread on carbon and silicon nitride membrane supports. Aberration-corrected HAADF-STEM was performed in a JEOL NeoARM instrument at 200 keV. Energy-dispersive X-ray spectroscopy (EDS) was carried out in an FEI Nova NanoSEM 450 field emission scanning electron microscope and an FEI Tecnai Osiris TEM at 200 kV. Second harmonic generation (SHG) measurements were conducted using a 50 fs Ti:Sapphire laser (Micra, Coherent) at 800 nm and 80 MHz repetition rate. The laser beam was passed through a half-wave plate mounted in a rotation stage, directed into an upright microscope (Olympus) and focused onto a nanowire using a 100× microscope objective (numerical aperture, NA = 0.9) to a ~1.5 μm spot. The laser energy at the sample surface was ~300 μW. SHG light was collected in backscattering configuration using the same objective and directed to a monochromator (Spectra Pro 2300i, Acton, f = 0.3 m, 150 grooves/mm grating) coupled to the microscope and a CCD camera (Pixis 256BR, Princeton Instruments). Before entering the monochromator, the SHG light was passed through a short-pass cut-off filter (650 nm) to filter out the fundamental excitation light at 800 nm and a polarizer to select the SHG polarization parallel to that of the exciting light. SHG mapping was performed by moving the sample using a computer controlled motorized XY stage with 0.2 μm steps and acquiring full spectra at each point (0.5 s acquisition time). To plot the maps, the SHG spectral lines at 400 nm were integrated from 390 nm to 410 nm at each pixel. Cathodoluminescence measurements were performed in HAADF-STEM at room temperature using a Gatan Vulcan CL holder and an incident electron beam current of 400 pA. Panchromatic CL maps were acquired with 512×512 pixels at 2 ms per pixel. Local spectra were obtained by positioning the exciting beam at selected locations within single nanowires and dispersing the emitted light in a spectrometer equipped with a cooled Si CCD detector (Integration time: 20 s).

Computational Methods: DFT calculations were carried out in the projector-augmented wave framework as implemented in VASP.[44-45] We used the exchange-correlation functional PBE-D2,[46-47] which we found to perform well in reproducing the experimental lattice parameters and heats of formation of tin chalcogenides in our previous work,[48] and also the lattice parameters of GeS and GeSe as shown in Table S1. An energy cutoff of 500 eV was used throughout and the Brillouin zone was sampled using a k-point mesh of 12x12x4 or larger. The calculated energy differences between A-B and A-A'/A-A phases are listed in Table S1. The A-A' phase consisting of staggered A-layers, which shows lower energy under most conditions (see Table S1), is in agreement with experimental TEM, STEM and electron diffraction results. The stacking fault models were constructed by taking n units of A-B phase

unit cells (with two layers each) and inserting a single additional layer with A-A' or A-A stacking. The stacking fault energy was calculated with respect to the same number of atoms of pristine A-B phase.

The electric polarization was calculated using the Berry phase expression within the modern theory of polarization,[49-50] which is defined only up to modulo $\mathbf{P}_m = e\mathbf{R}/\Omega$, where R is the lattice vector and Ω is the unit cell volume. To resolve this indeterminacy, we inspected the change in polarization along a path that connects the stacking fault structures of opposite orientation (see Figure 5 (a)) to find abrupt jumps corresponding to $\mathbf{P}_m$. Figure 5 (b) shows the polarization after these jumps have been removed. The switching path was constructed by first carrying out a nudged elastic band calculation with five intermediate images and then linearly interpolating three additional images between each of them.

The cluster expansion (CE) and special quasi-random structures (SQS) were constructed using ATAT package.[51-53] CE was fitted to 61 automatically generated structures. The CE contains only pair-interactions up to 11.7 Å distance and yields a cross-validation score 0.96 meV per X site (or per GeX formula unit). A comparison of CE and DFT energies is shown in Figure S13. The SQS were constructed using a 4x4x1 supercell and a 3x2x4 k-point mesh was used in the calculations.

Supporting Information: *Supporting Figures:* Structure of A-B, A-A, and A-A' stacked monochalcogenides; TEM of GeSe ribbons; SEM EDS maps and spectrum; additional TEM, STEM, and electron diffraction of $GeSe_{1-x}S_x$ alloy nanowires with stacking faults; aberration-corrected HAADF-STEM of stacking faults in $GeSe_{1-x}S_x$ alloy nanowires; TEM showing the persistence of stacking faults at higher S content; TEM of chiral twisted $GeSe_{1-x}S_x$ nanowires obtained for $x > 0.6$; EDS analysis of correlation between composition and stacking faults; TEM of a single-crystalline GeSe plate with stacking faults; measured *a*-lattice parameters of $GeSe_{1-x}S_x$ alloy nanowires; DFT results on the stability of $GeSe_{1-x}S_x$ alloys; computed lattice constants for $GeSe_{1-x}S_x$ alloys; optimized structures of A-B, A-A, and A-A' stacked monochalcogenides; stacking fault energies for different number of host layers and stacking fault layers; electronic density of states at A-A and A-A' stacking faults embedded in an A-B stacked host crystal; computation of ferroelectric polarization switching in a GeSe monolayer; cathodoluminescence spectroscopy of $GeSe_{1-x}S_x$ alloy nanowires; possibilities for polarization control in layered nanowires with polar inclusions. *Supporting Table:* Computed lattice parameters and energy differences for bulk GeS and GeSe with different stacking. *Supporting References* (PDF).

Acknowledgements

This work was supported by the National Science Foundation, Division of Materials Research, Solid State and Materials Chemistry Program under Grant No. DMR-1904843. EDS measurements were performed in the Nebraska Nanoscale Facility: National Nanotechnology Coordinated Infrastructure and the Nebraska Center for Materials and Nanoscience, which are supported by the National Science Foundation under Award ECCS: 2025298, and the Nebraska Research Initiative. SHG measurements and aberration-corrected STEM imaging were supported by the Center for Nanophase Materials Sciences (CNMS), which is a US Department of Energy, Office of Science User Facility at Oak Ridge National Laboratory. The authors acknowledge CSC – IT Center for Science, Finland, for computational resources.

Author Contributions

E.S. and P.S. designed the study and wrote the paper, with input from H.-P.K. P.S. synthesized the samples. E.S. carried out electron microscopy, diffraction, and cathodoluminescence experiments, which were jointly analyzed by E.S. and P.S. H.-P.K. performed the computational work, including DFT calculations and computations of electric polarization and layer switching. A.P. conducted the SHG measurements. R.R.U. performed aberration-corrected HAADF-STEM. SHG and STEM data were analyzed by P.S. and E.S. All authors read and commented on the manuscript.

References

1. Yuan, S.; Luo, X.; Chan, H. L.; Xiao, C.; Dai, Y.; Xie, M.; Hao, J. Room-Temperature Ferroelectricity in $MoTe_2$ Down to the Atomic Monolayer Limit. *Nature Communications* **2019**, *10*, 1775.
2. Zheng, C.; Yu, L.; Zhu, L.; Collins, J. L.; Kim, D.; Lou, Y.; Xu, C.; Li, M.; Wei, Z.; Zhang, Y.; Edmonds, M. T.; Li, S.; Seidel, J.; Zhu, Y.; Liu, J. Z.; Tang, W.-X.; Fuhrer, M. S. Room Temperature In-Plane Ferroelectricity in Van der Waals In_2Se_3. *Science Advances* **2018**, *4*, eaar7720.
3. Higashitarumizu, N.; Kawamoto, H.; Lee, C.-J.; Lin, B.-H.; Chu, F.-H.; Yonemori, I.; Nishimura, T.; Wakabayashi, K.; Chang, W.-H.; Nagashio, K. Purely In-Plane Ferroelectricity in Monolayer SnS at Room Temperature. *Nature Communications* **2020**, *11*, 2428.
4. Sutter, P.; Komsa, H. P.; Lu, H.; Gruverman, A.; Sutter, E. Few-Layer Tin Sulfide (SnS): Controlled Synthesis, Thickness Dependent Vibrational Properties, and Ferroelectricity. *Nano Today* **2021**, *37*, 101082.
5. Chang, K.; Küster, F.; Miller, B. J.; Ji, J.-R.; Zhang, J.-L.; Sessi, P.; Barraza-Lopez, S.; Parkin, S. S. P. Microscopic Manipulation of Ferroelectric Domains in SnSe Monolayers at Room Temperature. *Nano Letters* **2020**, *20*, 6590-6597.

6. Fei, Z.; Zhao, W.; Palomaki, T. A.; Sun, B.; Miller, M. K.; Zhao, Z.; Yan, J.; Xu, X.; Cobden, D. H. Ferroelectric Switching of a Two-Dimensional Metal. *Nature* **2018**, *560*, 336-339.
7. Suzuki, R.; Sakano, M.; Zhang, Y. J.; Akashi, R.; Morikawa, D.; Harasawa, A.; Yaji, K.; Kuroda, K.; Miyamoto, K.; Okuda, T.; Ishizaka, K.; Arita, R.; Iwasa, Y. Valley-Dependent Spin Polarization in Bulk MoS_2 with Broken Inversion Symmetry. *Nature Nanotechnology* **2014**, *9*, 611-617.
8. Shi, J.; Yu, P.; Liu, F.; He, P.; Wang, R.; Qin, L.; Zhou, J.; Li, X.; Zhou, J.; Sui, X.; Zhang, S.; Zhang, Y.; Zhang, Q.; Sum, T. C.; Qiu, X.; Liu, Z.; Liu, X. 3R MoS_2 with Broken Inversion Symmetry: A Promising Ultrathin Nonlinear Optical Device. *Advanced Materials* **2017**, *29*, 1701486.
9. Akamatsu, T.; Ideue, T.; Zhou, L.; Dong, Y.; Kitamura, S.; Yoshii, M.; Yang, D.; Onga, M.; Nakagawa, Y.; Watanabe, K.; Taniguchi, T.; Laurienzo, J.; Huang, J.; Ye, Z.; Morimoto, T.; Yuan, H.; Iwasa, Y. A Van der Waals Interface that Creates In-Plane Polarization and a Spontaneous Photovoltaic Effect. *Science* **2021**, *372*, 68-72.
10. Rogée, L.; Wang, L.; Zhang, Y.; Cai, S.; Wang, P.; Chhowalla, M.; Ji, W.; Lau, S. P. Ferroelectricity in Untwisted Heterobilayers of Transition Metal Dichalcogenides. *Science* **2022**, *376*, 973-978.
11. Yasuda, K.; Wang, X.; Watanabe, K.; Taniguchi, T.; Jarillo-Herrero, P. Stacking-Engineered Ferroelectricity in Bilayer Boron Nitride. *Science* **2021**, *372*, 1458-1462.
12. Vizner Stern, M.; Waschitz, Y.; Cao, W.; Nevo, I.; Watanabe, K.; Taniguchi, T.; Sela, E.; Urbakh, M.; Hod, O.; Shalom, M. B. Interfacial Ferroelectricity by Van der Waals Sliding. *Science* **2021**, *372*, 1462-1466.
13. Gomes, L. C.; Carvalho, A. Phosphorene Analogues: Isoelectronic Two-Dimensional Group-IV Monochalcogenides with Orthorhombic Structure. *Physical Review B* **2015**, *92*, 085406.
14. Wang, H.; Qian, X. Two-Dimensional Multiferroics in Monolayer Group IV Monochalcogenides. *2D Materials* **2017**, *4*, 015042.
15. Wu, M.; Zeng, X. C. Intrinsic Ferroelasticity and/or Multiferroicity in Two-Dimensional Phosphorene and Phosphorene Analogues. *Nano Letters* **2016**, *16*, 3236-3241.
16. Barraza-Lopez, S.; Kaloni, T. P.; Poudel, S. P.; Kumar, P. Tuning the Ferroelectric-to-Paraelectric Transition Temperature and Dipole Orientation of Group-IV Monochalcogenide Monolayers. *Physical Review B* **2018**, *97*, 024110.
17. Fei, R.; Kang, W.; Yang, L. Ferroelectricity and Phase Transitions in Monolayer Group-IV Monochalcogenides. *Physical Review Letters* **2016**, *117*, 097601.
18. Fei, R.; Li, W.; Li, J.; Yang, L. Giant Piezoelectricity of Monolayer Group IV Monochalcogenides: SnSe, SnS, GeSe, and GeS. *Applied Physics Letters* **2015**, *107*, 173104.
19. Hanakata, P. Z.; Carvalho, A.; Campbell, D. K.; Park, H. S. Polarization and Valley Switching in Monolayer Group-IV Monochalcogenides. *Physical Review B* **2016**, *94*, 035304.
20. Wu, M.; Zeng, X. C. Intrinsic Ferroelasticity and/or Multiferroicity in Two-Dimensional Phosphorene and Phosphorene Analogues. *Nano Letters* **2016**, *16*, 3236−3241.
21. Bao, Y.; Song, P.; Liu, Y.; Chen, Z.; Zhu, M.; Abdelwahab, I.; Su, J.; Fu, W.; Chi, X.; Yu, W.; Liu, W.; Zhao, X.; Xu, Q.-H.; Yang, M.; Loh, K. P. Gate-Tunable In-Plane Ferroelectricity in Few-Layer SnS. *Nano Letters* **2019**, *19*, 5109-5117.

22. Kwon, K. C.; Zhang, Y.; Wang, L.; Yu, W.; Wang, X.; Park, I.-H.; Choi, H. S.; Ma, T.; Zhu, Z.; Tian, B.; Su, C.; Loh, K. P. In-Plane Ferroelectric Tin Monosulfide and Its Application in a Ferroelectric Analog Synaptic Device. *ACS Nano* **2020**, *14*, 7628-7638.
23. Sutter, E.; Wang, J.; Sutter, P. Surface Passivation by Excess Sulfur for Controlled Synthesis of Large, Thin SnS Flakes. *Chemistry of Materials* **2020**, *32*, 8034-8042.
24. Sutter, E.; Zhang, B.; Sun, M.; Sutter, P. Few-Layer to Multilayer Germanium(II) Sulfide: Synthesis, Structure, Stability, and Optoelectronics. *ACS Nano* **2019**, *13*, 9352-9362.
25. Vaughn, D. D.; Patel, R. J.; Hickner, M. A.; Schaak, R. E. Single-Crystal Colloidal Nanosheets of GeS and GeSe. *Journal of the American Chemical Society* **2010**, *132*, 15170-15172.
26. Zhou, X.; Hu, X.; Jin, B.; Yu, J.; Liu, K.; Li, H.; Zhai, T. Highly Anisotropic GeSe Nanosheets for Phototransistors with Ultrahigh Photoresponsivity. *Advanced Science* **2018**, *5*, 1800478.
27. Xia, J.; Li, X.-Z.; Huang, X.; Mao, N.; Zhu, D.-D.; Wang, L.; Xu, H.; Meng, X.-M. Physical Vapor Deposition Synthesis of Two-Dimensional Orthorhombic SnS Flakes with Strong Angle/Temperature-Dependent Raman Responses. *Nanoscale* **2016**, *8*, 2063-2070.
28. Lan, C.; Li, C.; Yin, Y.; Guo, H.; Wang, S. Synthesis of Single-Crystalline GeS Nanoribbons for High Sensitivity Visible-Light Photodetectors. *Journal of Materials Chemistry C* **2015**, *3*, 8074-8079.
29. Sutter, P.; Wimer, S.; Sutter, E. Chiral Twisted Van der Waals Nanowires. *Nature* **2019**, *570*, 354-357.
30. Sutter, E.; Sutter, P. 1D Wires of 2D Layered Materials: Germanium Sulfide Nanowires as Efficient Light Emitters. *ACS Applied Nano Materials* **2018**, *1*, 1042-1049.
31. Im, H. S.; Myung, Y.; Park, K.; Jung, C. S.; Lim, Y. R.; Jang, D. M.; Park, J. Ternary Alloy Nanocrystals of Tin and Germanium Chalcogenides. *RSC Advances* **2014**, *4*, 15695-15701.
32. Sutter, P.; Khorashad, L. K.; Argyropoulos, C.; Sutter, E. Cathodoluminescence of Ultrathin Twisted $Ge_{1-x}Sn_xS$ van der Waals Nanoribbon Waveguides. *Advanced Materials* **2021**, *33*, 2006649.
33. Wu, F.; Zhang, R.-X.; Das Sarma, S. Three-Dimensional Topological Twistronics. *Physical Review Research* **2020**, *2*, 022010.
34. Murgatroyd, P. A. E.; Smiles, M. J.; Savory, C. N.; Shalvey, T. P.; Swallow, J. E. N.; Fleck, N.; Robertson, C. M.; Jäckel, F.; Alaria, J.; Major, J. D.; Scanlon, D. O.; Veal, T. D. GeSe: Optical Spectroscopy and Theoretical Study of a van der Waals Solar Absorber. *Chemistry of Materials* **2020**, *32*, 3245-3253.
35. Solanki, G. K.; Deshpande, M. P.; Agarwal, M. K.; Patel, P. D.; Vaidya, S. N. Thermoelectric Power Factor Measurements in GeSe Single Crystals Grown Using Different Transporting Agents. *Journal of Materials Science Letters* **2003**, *22*, 985-987.
36. Sutter, E.; French, J. S.; Sutter, P. Free-Standing Large, Ultrathin Germanium Selenide van der Waals Ribbons by Combined Vapor-Liquid-Solid Growth and Edge Attachment. *Nanoscale* **2022**, *14*, 6195-6201
37. Sutter, P.; French, J. S.; Khosravi Khorashad, L.; Argyropoulos, C.; Sutter, E. Optoelectronics and Nanophotonics of Vapor–Liquid–Solid Grown GaSe van der Waals Nanoribbons. *Nano Letters* **2021**, *21*, 4335-4342.
38. Sutter, E.; French, J. S.; Sutter, S.; Idrobo, J. C.; Sutter, P. Vapor–Liquid–Solid Growth and Optoelectronics of Gallium Sulfide van der Waals Nanowires. *ACS Nano* **2020**, *14*, 6117-6126.

39. Onodera, A.; Sakamoto, I.; Fujii, Y.; Mo⁄ri, N.; Sugai, S. Structural and electrical properties of GeSe and GeTe at high pressure. *Physical Review B* **1997**, *56*, 7935-7941.
40. Wiedemeier, H.; Schnering, H. G. V. Refinement of the Structures of GeS, GeSe, SnS and SnSe. *Z Kristallogr* **1978**, *148*, 295-303.
41. Sutter, E. A.; Sutter, P. W.; Uccelli, E.; Fontcuberta i Morral, A. Supercooling of Nanoscale Ga Drops With Controlled Impurity Levels. *Physical Review B* **2011**, *84*, 193303.
42. Sutter, P.; Idrobo, J.-C.; Sutter, E. Van der Waals Nanowires with Continuously Variable Interlayer Twist and Twist Homojunctions. *Advanced Functional Materials* **2021**, *31*, 2006412.
43. Sutter, E.; French, J. S.; Sutter, P. Tunable Layer Orientation and Morphology in Vapor–Liquid–Solid Growth of One-Dimensional GeS van der Waals Nanostructures. *Chemistry of Materials* **2021**, *33*, 3980-3988.
44. Kresse, G.; Furthmüller, J. Efficient Iterative Schemes for Ab Initio Total-Energy Calculations Using a Plane-Wave Basis Set. *Physical Review B* **1996**, *54*, 11169-11186.
45. Kresse, G.; Joubert, D. From Ultrasoft Pseudopotentials to the Projector Augmented-Wave Method. *Physical Review B* **1999**, *59*, 1758-1775.
46. Perdew, J. P.; Burke, K.; Ernzerhof, M. Generalized Gradient Approximation Made Simple. *Physical Review Letters* **1997**, *78*, 1396-1396.
47. Grimme, S. Semiempirical GGA-Type Density Functional Constructed with a Long-Range Dispersion Correction. *Journal of Computational Chemistry* **2006**, *27*, 1787-1799.
48. Sutter, E.; Huang, Y.; Komsa, H. P.; Ghorbani-Asl, M.; Krasheninnikov, A. V.; Sutter, P. Electron-Beam Induced Transformations of Layered Tin Dichalcogenides. *Nano Letters* **2016**, *16*, 4410-4416.
49. King-Smith, R. D.; Vanderbilt, D. Theory of Polarization of Crystalline Solids. *Physical Review B* **1993**, *47*, 1651-1654.
50. Resta, R. Macroscopic Polarization in Crystalline Dielectrics: the Geometric Phase Approach. *Reviews of Modern Physics* **1994**, *66*, 899-915.
51. van de Walle, A.; Ceder, G. Automating First-principles Phase Diagram Calculations. *Journal of Phase Equilibria* **2002**, *23*, 348.
52. van de Walle, A. Multicomponent Multisublattice Alloys, Nonconfigurational Entropy and Other Additions to the Alloy Theoretic Automated Toolkit. *Calphad* **2009**, *33*, 266-278.
53. van de Walle, A.; Asta, M. Self-Driven Lattice-Model Monte Carlo Simulations of Alloy Thermodynamic Properties and Phase Diagrams. *Modelling and Simulation in Materials Science and Engineering* **2002**, *10*, 521-538.

TOC Graphic